ACS APPLIED MATERIALS & INTERFACES
Research Article
www.acsami.org

# Effects of Nitrogen Incorporation in $HfO_2$ Grown on InP by Atomic Layer Deposition: An Evolution in Structural, Chemical, and Electrical Characteristics

Yu-Seon Kang,[†] Dae-Kyoung Kim,[†] Hang-Kyu Kang,[†] Kwang-Sik Jeong,[†] Mann-Ho Cho,*[,†] Dae-Hong Ko,[‡] Hyoungsub Kim,[§] Jung-Hye Seo,[∥] and Dong-Chan Kim[⊥]

[†]Institute of Physics and Applied Physics, Yonsei University, Seoul 120-749, Korea

[‡]Department of Material Science and Engineering, Yonsei University, Seoul 120-749, Korea

[§]School Department of Material Science and Engineering, Sungkyunkwan University, Suwon 440-746, Korea

[∥]Analysis and Research Division, Korea Basic Science Institute, Daejeon 305-806, Korea

[⊥]Process Development Team, Semiconductor R&D Center, Samsung Electronics Co., Ltd., Yongin 446-711, Korea

Supporting Information

**ABSTRACT:** We investigated the effects of postnitridation on the structural characteristics and interfacial reactions of $HfO_2$ thin films grown on InP by atomic layer deposition (ALD) as a function of film thickness. By postdeposition annealing under $NH_3$ vapor (PDN) at 600 °C, an InN layer formed at the $HfO_2$/InP interface, and ionized $NH_x$ was incorporated in the $HfO_2$ film. We demonstrate that structural changes resulting from nitridation of $HfO_2$/InP depend on the film thickness (i.e., a single-crystal interfacial layer of *h*-InN formed at thin (2 nm) $HfO_2$/InP interfaces, whereas an amorphous InN layer formed at thick (>6 nm) $HfO_2$/InP interfaces). Consequently, the tetragonal structure of $HfO_2$ transformed into a mixture structure of tetragonal and monoclinic because the interfacial InN layer relieved interfacial strain between $HfO_2$ and InP. During postdeposition annealing (PDA) in $HfO_2$/InP at 600 °C, large numbers of oxidation states were generated as a result of interfacial reactions between interdiffused oxygen impurities and out-diffused InP substrate elements. However, in the case of the PDN of $HfO_2$/InP structures at 600 °C, nitrogen incorporation in the $HfO_2$ film effectively blocked the out-diffusion of atomic In and P, thus suppressing the formation of oxidation states. Accordingly, the number of interfacial defect states ($D_{it}$) within the band gap of InP was significantly reduced, which was also supported by DFT calculations. Interfacial InN in $HfO_2$/InP increased the electron-barrier height to ∼0.6 eV, which led to low-leakage-current density in the gate voltage region over 2 V.

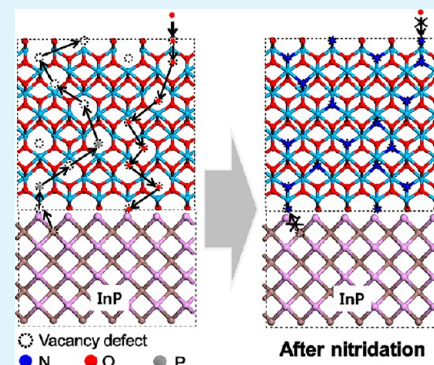


**KEYWORDS:** *thin films, indium phosphide, nitridation, band alignment*

## I. INTRODUCTION

In the semiconductor industry, $SiO_2$/Si-based complementary metal-oxide semiconductor (MOS) technology has reached its fundamental physical limits, as evidenced by poor reliability, high-frequency dispersion, and high-leakage-currents problems. Advanced gate-stacked MOS structures based on high-$\kappa$ oxides and III−V compound semiconductors are being considered for use in future MOS device applications because of their high mobility and low power consumption compared to Si. Among the many promising candidates for high-$\kappa$/III−V structures, $HfO_2$/InP has moderate band offsets and excellent electrical properties that are acceptable for use in MOS devices.[1−3] In particular, $HfO_2$ grown on InP by atomic layer deposition (ALD) has a high-quality interface without In and P oxidation states through a self-cleaning effect.[4,5] However, the $HfO_2$/InP system has poor thermal stability; In or P can diffuse into the $HfO_2$ film during the postannealing process, which leads to a large amount of interfacial traps and oxide charge traps.[6,7] To enhance the thermal stability of the $HfO_2$/InP system for advanced MOS applications, process optimization is required. Recently, $SF_6$ plasma treatment of $HfO_2$/InP was proposed because incorporation of S and F in a $HfO_2$ film can improve drive current and channel mobility.[8] In addition, incorporation of Al into $HfO_2$ to generate a $Hf_xAl_yO$ film on InP enhanced the electrical properties of the resultant film by suppression of In and P diffusion.[9] Moreover, nitrogen substitution in the high-$\kappa$/GaAs interface has been proposed as another process to minimize interfacial diffusion and defect states. Robertson et al. calculated the electronic structure of the nitrogen-substituted $Al_2O_3$/GaAs interface using density functional theory and found that the inevitable generation of defects in the interface

**Received:** November 5, 2013
**Accepted:** January 27, 2014
**Published:** January 27, 2014

ACS Publications © 2014 American Chemical Society

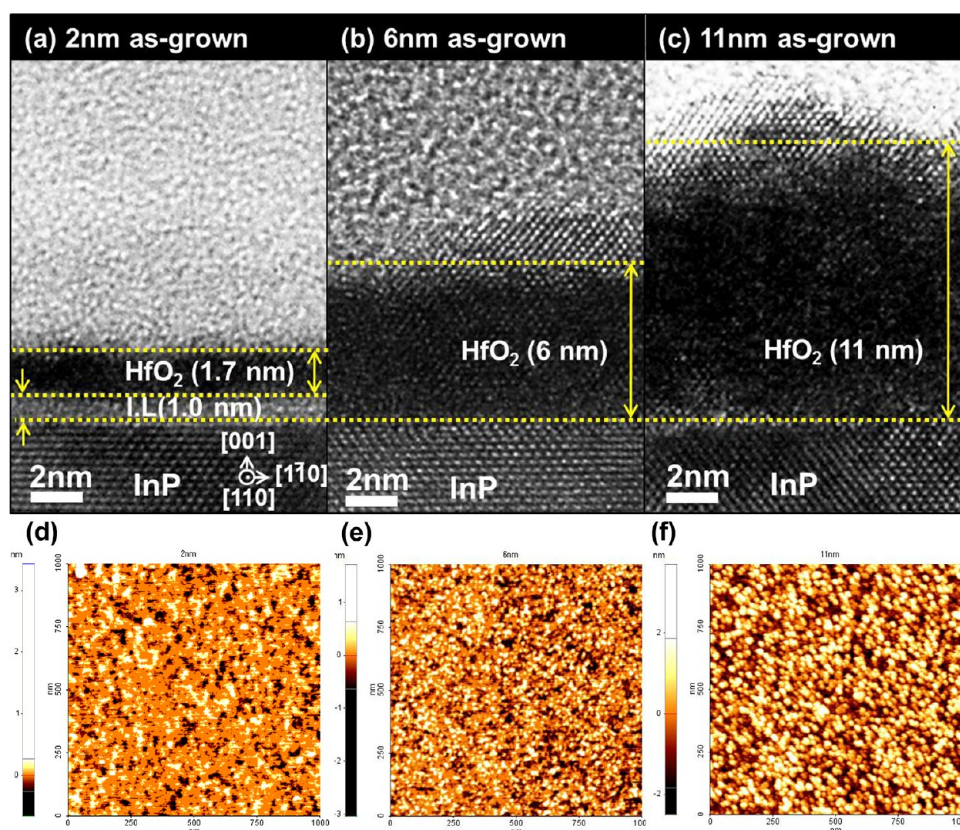


**Figure 1.** Cross-sectional HR-TEM images of as-grown $HfO_2$ film on InP as a function of film thickness: (a) 2, (b) 6, and (c) 11 nm $HfO_2$. Atomic force microscopy of (d) 2, (e) 6, and (f) 11 nm thick $HfO_2$ film on InP with a scale bar of $1 \times 1$ $\mu m^2$.

of $Al_2O_3$/GaAs can be suppressed by nitrogen incorporation because of effective passivation of nitrogen at the interface.[10]

In this study, we performed nitridation in $HfO_2$/InP using rapid thermal annealing in $NH_3$ vapor. We investigated the effects of incorporation of nitrogen in $HfO_2$/InP on the structural, chemical, and electrical properties of the resultant film as well as its thermal stability compared to samples that were only thermally annealed by comprehensive physical, electrical, and theoretical analyses. We observed that nitridation can significantly improve the electrical properties of $HfO_2$/InP, such as their leakage current and defect states. We examined the origins of the improved electrical properties of the nitrided $HfO_2$/InP system systemically by analyzing the (i) crystalline structure, (ii) energy-band alignment, (iii) interfacial reaction, and (iv) defect states of nitrided $HfO_2$/InP.

## II. EXPERIMENTAL SECTION

$HfO_2$ films with three different thicknesses (approximately 2, 6, and 11 nm) were deposited on n-InP (001) substrate (doping concentration $\sim 7 \times 10^{17}$ $cm^{-3}$) by atomic layer deposition (ALD). Before deposition of the $HfO_2$ films, the InP substrate was cleaned in a dilute solution (~ 1%) of buffed oxide etchant (BOE, $NH_4F$/HF = 6:1) for 5 min. Then, the substrate was rinsed in deionized $H_2O$ and dried by blowing $N_2$ over the substrate. The chemically etched substrate was transferred immediately to the ALD chamber. Tetrakis(ethylmethylamido) hafnium $Hf[N(CH_3)(C_2H_5)]_4$ (TEMAHf) and $H_2O$ vapor were used as the Hf metal precursor and oxygen source, respectively, followed by a $N_2$ purging step: TEMAHf (2 s) → $N_2$ (10 s) → $H_2O$ (1.5 s) → $N_2$ (15 s) represented one cycle. The flow rates of TEMAHf-carrying $N_2$ and $H_2O$ were 10 and 50 sccm, respectively, and that of the purging $N_2$ was 200 sccm. The growth rate of $HfO_2$ in our ALD system was ~0.78 Å/cycle. We performed 26, 77, and 141 cycles of ALD to deposit the $HfO_2$ film to achieve a film thickness of 2, 6, and 11 nm, respectively. Films were annealed at 600 °C by a rapid thermal process for 1 min in an environment of $N_2$ (PDA) or $NH_3$ (PDN).

Microstructure of the $HfO_2$ films on InP was investigated using high-resolution transmission electron microscopy (HRTEM) and X-ray diffraction (XRD). Surface morphology of the films was evaluated using atomic force microscopy (AFM). Energy band gaps of the $HfO_2$ films were measured by reflection electron energy-loss spectroscopy (REELS) with a primary electron-beam energy of 1.0 keV. Valence band analysis and interfacial chemistry of $HfO_2$ films grown on InP were examined by high-resolution X-ray photoelectron spectroscopy (XPS) using a monochromatic Al K$\alpha$ X-ray source ($h\nu$ = 1486.7 eV) with a pass energy of 20 eV. InP substrate was electrically grounded to the electron analyzer to eliminate charging effects. Binding energy of measured core-level spectra of C 1s, Hf 4f (In 4d), In 3d, P 2p, and N 1s were calibrated by core-level spectra using the C 1s spectrum (surface carbon, 284.9 eV for the C−H bond). To deconvolute the XPS core-level spectra, background was removed by Shirley-type subtraction, and full-width at half maximum (fwhm) values of the constituent peaks were kept constant. We obtained a fwhm value of under 0.43 eV for Ag $3d_{5/2}$ core-level spectra. Fitting curves were determined by Gaussian and Lorentzian distributions in which the Gaussian distribution ratio was higher than 80%. In addition, for the case of the Hf 4f, In 3d, and P 2p doublets, the intensity ratio of the doublet caused by spin−orbit splitting was determined by the transition probability during photoionization. To examine the electrical characteristics of the films, a metal-oxide semiconductor capacitor (MOSCAP) with a sputter-deposited TiN top electrode with an area of $6.4 \times 10^{-5}$ $cm^2$ area and thickness of 600 nm was fabricated via a lift-off technique. Forming gas annealing (defect-curing process) was not carried out because of accurate defect analysis. Capacitance−voltage ($C-V$) and leakage-current characteristics were measured using an Agilent E4980A LCR meter and an Agilent B1500A semiconductor device analyzer, respectively. To compare the interface


dx.doi.org/10.1021/am4049496 | ACS Appl. Mater. Interfaces 2014, 6, 3896−3906

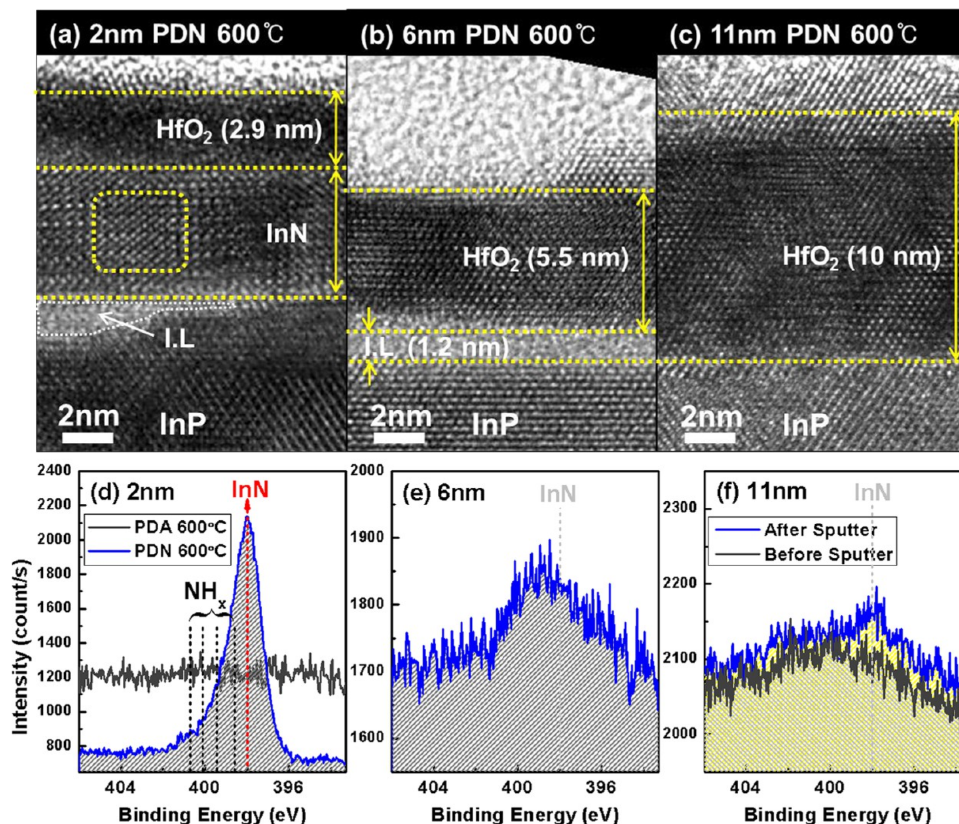


**Figure 2.** Cross-sectional HR-TEM images of $HfO_2$ film on InP after rapid thermal annealing in a $NH_3$ ambient at 600 °C as a function of film thickness: (a) 2, (b) 6, and (c) 11 nm $HfO_2$. XPS N 1s core-level spectra of annealed (d) 2, (e) 6, and (f) 11 nm $HfO_2$ on InP with a takeoff angle of 54.7°. In the N 1s spectra, the peak at 398 eV corresponds to InN.

trap density ($D_{it}$) of $HfO_2$/InP before and after thermal annealing, capacitance ($C_m$) and conductance ($G_m$) were measured. The density of the interfacial defect state ($D_{it}$) was determined by parallel conductance $(G_p/\omega)_{max}$, and the energy level of the defect state was determined from frequency measurements. Trap energy level given by Shockley−Read−Hall statistics for the capture and emission rates was evaluated using the following equation, which describes the relationship between the time constant, $\tau$, of the trap and the frequency

$$f = \frac{1}{2\pi\tau} = \frac{v_{th}\sigma N}{2\pi}\exp\left[\frac{-\Delta E}{k_B T}\right]$$

where $v_{th}$ is the average thermal velocity of the majority carrier, $N$ is the effective density of states of the majority carrier, and $\sigma$ is the captured cross-section of the trap state. The $G_p/\omega$ value was calculated using the following equation[11]

$$\frac{G_p}{\omega} = \frac{\omega C_{ox}{}^2 G_m}{[G_m{}^2 + \omega^2(C_{ox} - C_m)^2]}$$

where $\omega$ is $2\pi f$, and frequency ($f$) is measured from 1 kHz to 1 MHz. $C_{ox}$ is the gate oxide capacitance, and $G_m$ and $C_m$ are the measured conductance and capacitance, respectively. $D_{it}$ in depletion is proportional to the peak values of $G_p/\omega$

$$D_{it} \approx 2.5\frac{(G_p/\omega)_{max}}{Aq}$$

where $A$ is the area of the electrode and $q$ is the elemental charge.

In addition, we employed density functional theory (DFT) calculations to understand the origin of interfacial defect states using supercell models. Local structure and formation energy were calculated using VASP code with the exchange correlation function of the generalized gradient approximation (GGA) PBESol. Geometry optimization for the unit cell of the *P42/nmc* $HfO_2$ structure was performed. The conventional cell for $HfO_2$ was calculated using 7 × 7 × 7 *k*-points. To minimize interactions between charged defects, 3 × 3 × 2 ($HfO_2$) supercells were used for defect calculations. Gamma *k*-points for geometry optimization and 3 × 3 × 3 *k*-points were used to calculate the energy state and density of states, respectively. All calculations were carried out using a plane wave cutoff energy of 500 eV.

## III. RESULTS AND DISCUSSION

Cross-sectional high-resolution transmission electron microscopy (HR-TEM) images of $HfO_2$ films on InP as a function of film thickness are shown in Figure 1. The thicknesses of $HfO_2$ films without an interfacial layer were approximately 2, 6, and 11 nm, respectively. An interfacial layer of ∼1 nm was observed for 2 nm thick $HfO_2$/InP, whereas no interfacial layer was observed for either 6 or 11 nm thick $HfO_2$/InP. Previous reports showed that a clean interface can be achieved by wet-cleaning and self-cleaning during the ALD process (i.e., the metal organic precursor (TEMAHf) consumed the native oxide effectively during the first few ALD cycles).[12,13] On the basis of the reported self-cleaning data, we expected that the native oxide in the 2 nm thick $HfO_2$/InP would be removed entirely during the ALD process. However, reoxidation by interdiffused oxygen occurred immediately upon air exposure, resulting in the formation of an ∼1 nm interfacial layer. McDonnell et al. recently reported interfacial oxide regrowth in a high-$\kappa$/GaAs system as a function of air-exposure time.[14] They speculated that air exposure after the ALD process is the main cause for interfacial oxide regrowth in a thin film (<2 nm). This is consistent with the changes we observed in interfacial oxide thickness as a function of film thickness. We also observed that

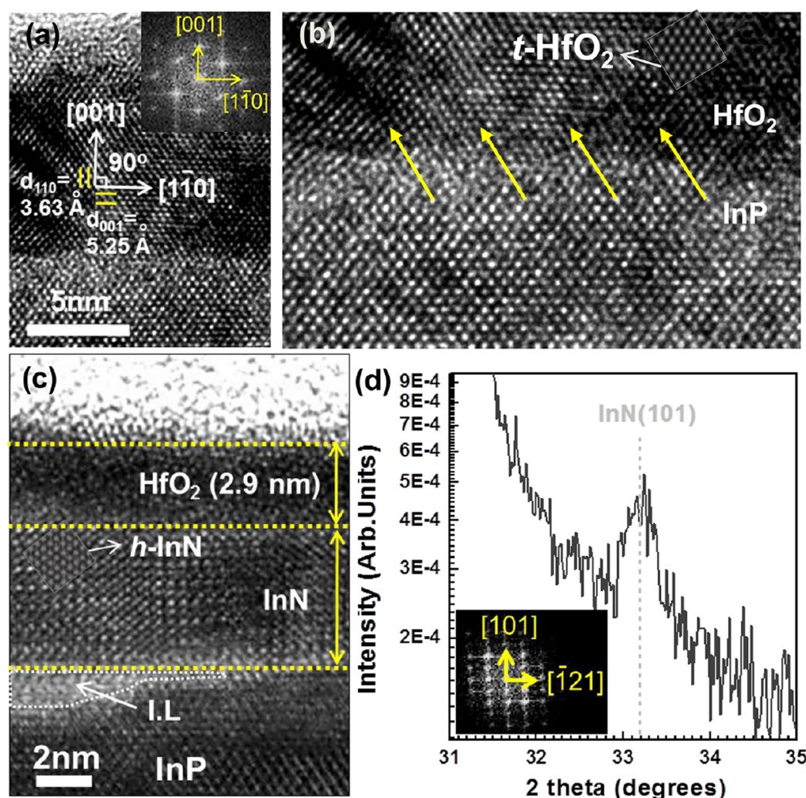


**Figure 3.** (a) HR-TEM images of as-grown 11 nm $HfO_2$ film on InP. The inset shows a fast Fourier transform (FFT) image of the 11 nm $HfO_2$ film. (b) Lattice mismatch between as-grown 11 nm $HfO_2$ film and the InP substrate. (c) HR-TEM images and (d) XRD result of the 2 nm $HfO_2$ film on InP after rapid thermal nitridation. The inset in panel d shows the FFT image for 2 nm $HfO_2$ on InP after PDN.

crystalline growth in the $HfO_2$ film and surface roughness of the $HfO_2$ film were related to film thickness. In other words, crystallization of the $HfO_2$ film increased gradually with increasing film thickness: partial crystallization in the 2 nm thick film, gradually increased crystallization in the 6 nm thick film, and full crystallization in the 11 nm thick film. We confirmed the surface roughness of the $HfO_2$ film by AFM surface topography as shown in Figure 1d−f: root-mean-square (rms) values for surface roughness were 0.157, 0.324, and 0.927 nm for the 2, 6, and 11 nm thick films, respectively. This indicates that crystalline growth during the ALD process increased surface roughness.

A drastic change in the $HfO_2$/InP structure was observed after rapid thermal nitridation (PDN), as shown in Figure 2. During PDN at 600 °C, a thick crystalline interfacial layer was produced at the interface between the 2 nm thick $HfO_2$/InP sample, and an amorphous interfacial layer appeared at the interface of the 6 nm sample, as shown in Figure 2a,b. In contrast, no interfacial layer was observed in the 11 nm thick $HfO_2$/InP sample. Confirmation of a very thin local interfacial oxide layer using TEM is difficult because observing a change in contrast and obtaining a clear image of a thin interfacial layer between the oxide film and the substrate is dependent on the TEM measurement conditions. To collect detailed information about the interfacial layer and to confirm the chemical states of the interfacial layer, we performed XPS measurements. XPS N 1s core-level spectra as a function of film thickness are shown in Figure 2d−f. The InN peak at 398.05 eV was observed in both the 2 and 6 nm thick samples after PDN, which clearly supports the formation of a nitride interfacial layer.[15,16] The 11 nm thick $HfO_2$ film was too thick to examine the interface; the penetration depth of photo electrons in $HfO_2$ is only about ~8 nm. Therefore, we performed ion sputtering to verify the interfacial chemical states. To minimize sputtering damage, the pressure of Ne gas, which is a light gas, was controlled at 5 mPa, and a sputtering power of 1 kV was maintained for 4 min. No interfacial layer was detected in the 11 nm thick sample after PDN on the basis of HR-TEM examination; however, an InN peak was clearly detected after sputtering on the basis of XPS analysis, as shown in Figure 2 f. This result indicates that InN formed during PDN even at the interface of the 11 nm thick $HfO_2$/InP sample. Moreover, we observed that ionized $NH_x$ states between 399 and 401 eV were present in all samples after PDN.[15] Elemental distribution in the depth direction was identified using time-of-flight secondary ion mass spectroscopy (TOF-SIMS). Nitrogen was observed throughout the $HfO_2$ film, as shown in Supporting Information Figure 1. That is, ionized $NH_x$ states formed throughout the film in the depth direction.

To understand mechanisms for structural changes of the $HfO_2$ film and interface in detail, HR-TEM measurement was carried out, as shown in Figure 3. The fully crystalline nature of the 11 nm thick $HfO_2$ film after ALD was confirmed by the HR-TEM images shown in Figure 3a,b. We obtained a *d*-spacing value of 5.25 Å for the film growth direction and 7.27 Å for the direction parallel to the substrate, which correspond to tetragonal (001) and tetragonal (110), respectively. In addition, using the NCEMSS simulator, we identified a simulated tetragonal structure at the (101) zone axis, as shown in the inset of Figure 3b. On the basis of the orientation relationship between *t*-$HfO_2$/InP in the HRTEM images, the atomic arrangement is *t*-$HfO_2$[110]‖InP[110] and *t*-$HfO_2$[1−

10]||InP[1−10]. Moreover, eight atoms of *t*-$HfO_2$ (110) matched with seven atoms of InP substrate, as shown by the yellow arrows in Figure 3b. The estimated interfacial lattice mismatch between *t*-$HfO_2$ film and InP substrate was about 0.10% for *t*-$HfO_2$/InP {⟨*t*-$HfO_2$ (110)⟩ = 7.27 Å, 7.27 Å × 8 = 58.16 Å and ⟨InP (110)⟩ = 8.3 Å, 8.3 Å × 7 = 58.10 Å}, resulting in minimization of interfacial energy.[5] There was a significant change in the film structure of the 2 nm thick $HfO_2$ sample after PDN. The thickness of the $HfO_2$ film increased by more than ∼1 nm compared to the as-grown film, and a thick crystalline interfacial layer with the chemical composition of InN formed, as confirmed by XPS. The crystalline structure and growth direction of the InN layer were examined by XRD, as shown in Figure 3d. We attributed the diffraction peak position at 33.18° to the hexagonal phase InN (101) structure, consistent with the TEM image showing a single-crystalline hexagonal structure at the (11−1) zone axis as identified by the NCEMSS simulator (Figure 3c). Considering the orientation relationship between *h*-InN/InP from the HR-TEM and XRD images, the atomic arrangement corresponds to *h*-InN[11−1]||InP[110] and *h*-InN [−121]||InP[1−10]. The estimated interfacial lattice mismatch between *h*-InN and the InP substrate was about 0.805%, indicating that crystalline growth of InN with a hexagonal structure was affected by interfacial strain, which served to minimize the interfacial energy.[15]

In contrast, the interfacial structure was drastically damaged after PDA in the 2 nm thick sample (i.e., many wide holes in the region of the substrate and some rough layers with an islandlike shape appeared on top of the film surface after PDA at 600 °C), as shown in the inset of Figure S2. The islandlike layer on the film surface was composed of In, P, and O, as confirmed by EDS at the position indicated with a white arrow (EDS data are not reported in this article), indicating that In and P that dissociated from the substrate regrew on top of the film surface. The thickness of the $HfO_2$ film in the 2 nm thick $HfO_2$/InP system after PDA at 500 °C was twice that of as-grown $HfO_2$ film, as shown in Figure S2a. In addition, the thickness of the 6 and 11 nm thick $HfO_2$/InP after PDA at 600 °C increased slightly, as shown in Figures 2b,c and S2b,c. Generally, densification because of crystallization decreases the film thickness after annealing. Therefore, the increase in film thickness indicates the generation of another layer during the annealing process. According to the TOF-SIMS results, out-diffusion of In and P after PDA at 600 °C increased the thickness of the $HfO_2$ film, as shown in Figure S1. The ∼50% increase in film thickness observed in 2 nm thick $HfO_2$ after PDN600 likely resulted from interfacial reaction via out-diffusion of InP substrate elements.

Figure 4 shows XRD data as a function of film thickness and postannealing conditions. In comparison with as-grown samples, the crystalline structure of $HfO_2$ film transformed from monoclinic to tetragonal when the film thickness increased (i.e., the monoclinic structure in 2 nm thick $HfO_2$ film was transformed to a tetragonal structure in 6 nm thick $HfO_2$ film). Only the tetragonal structure remained when the film thickness of $HfO_2$ was increased to 11 nm. In particular, *m* (−121) shifted ∼0.2° toward a lower diffraction angle as the film thickness increased from 2 to 6 nm. The peak shift toward a lower diffraction angle indicates that the interplanar distance increased and that the films were affected by compressive stress. We calculated the lattice mismatch in the case of *m*-$HfO_2$ contacting the InP substrate directly. Detailed growth orientation was determined from XRD data for film growth

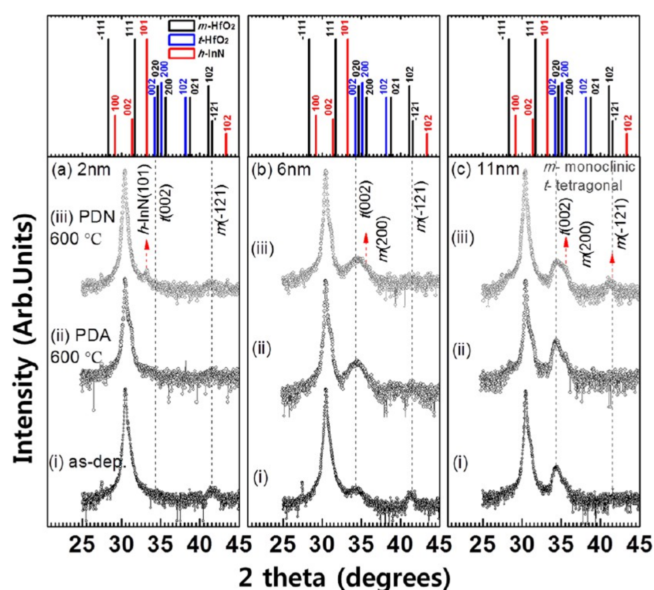


**Figure 4.** XRD data for (a) 2, (b) 6, and (c) 11 nm $HfO_2$ film on InP before and after annealing treatment. The peak positions of 30.43, 34.2, and 41.63° correspond to InP (002), tetragonal structure of $HfO_2$ (002), and the monoclinic structure of $HfO_2$ (−121), respectively. The red arrow at 36° indicates the monoclinic structure of $HfO_2$ (200). In the standard XRD peak position data, the black, blue, and red lines represent *m*-$HfO_2$, *t*-$HfO_2$, and *h*-InN, respectively.

direction and TEM data for the zone axis. Using the atomic arrangement of *m*-$HfO_2$ with the InP substrate, we determined the following growth directions: *m*-$HfO_2$[101]||InP[110] and *m*-$HfO_2$[11−1]||InP[1−10], resulting in a relatively high interfacial strain with a lattice mismatch of ∼0.52% compared to that of *t*-$HfO_2$ on InP. Therefore, phase transformation from monoclinic to tetragonal decreases interfacial strain from 0.52 to 0.10%. The peak of *t* (001) became broad and shifted toward a higher diffraction angle in both the 6 and 11 nm thick films after PDN. In addition, after PDN, *m* (200) and *m* (−121) structures appeared, as shown in Figure 4b,c. The mixture monoclinic and tetragonal structure obtained after PDN was due to the formation of an InN layer between $HfO_2$/InP by interfacial reactions. Several previous reports of high-κ/III−V semiconductors have reported a higher incidence of the *m*-$HfO_2$ structure than *t*-$HfO_2$ because *m*-$HfO_2$ has a lower heat of formation energy than *t*-$HfO_2$ (heat of formation energy of *m*-$HfO_2$ and *t*-$HfO_2$ is −1239.3 and −1228.6 kJ/mol, respectively).[17] However, in the $HfO_2$/InP system, *m*-$HfO_2$ transformed to *t*-$HfO_2$ to minimize interfacial lattice mismatch, as discussed earlier. After PDN, the inserted InN layer between the $HfO_2$ and InP changed the interfacial strain, resulting in a mixture structure.

To examine the detailed chemical states in $HfO_2$/InP before and after nitridation, XPS measurements were taken. Figure 5 shows In 3d and Hf 4f /In 4d core-level spectra as a function of film thickness. Multiple oxidation states of $In_2O_3$ at 444.7 eV, $In(PO_3)_3$ at 445.4 eV, and $InPO_4$ at 445.7 eV were deconvoluted from the In 3d spectra. Oxidation states were drastically increased in both the 6 and 11 nm thick $HfO_2$/InP after PDA compared to the films obtained after PDN. The formation of oxidation states in In 3d can be explained by interfacial reactions between interdiffused oxygen and the InP substrate. However, if these interfacial reactions occurred uniformly in limited interfacial regions, the oxidation states of

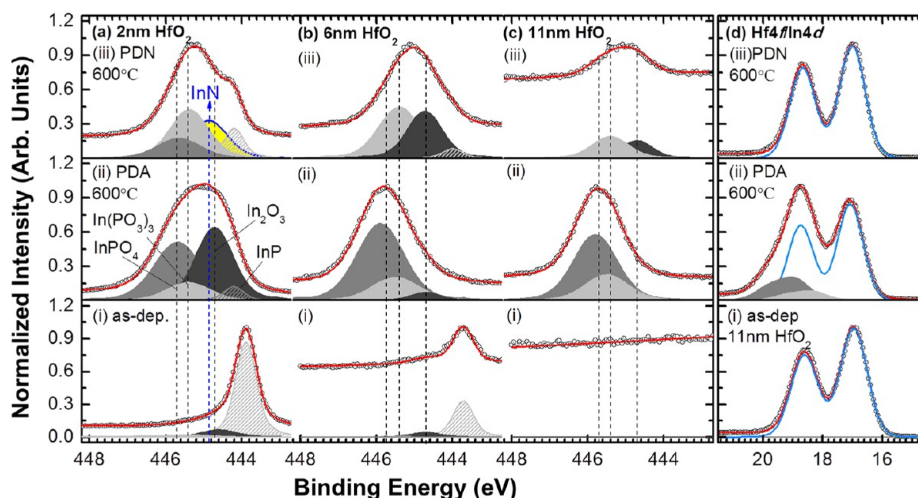


**Figure 5.** (a−c) XPS In 3d core-level spectra as a function of film thickness and annealing conditions. (d) XPS Hf 4f/In 4d core-level spectra of the 11 nm $HfO_2$ film on InP before and after annealing. In the In 3d spectra, the InP, $In_2O_3$, $In(PO_3)_3$, and $InPO_4$ bonding states correspond to binding energies of 444.4, 444.7, 445.4, and 445.7 eV, respectively.

the interfacial layer between the 11 nm thick $HfO_2$ film and InP substrate would not be detected because photoelectron yield decreases exponentially along the depth direction. In addition, HR-TEM results of the abrupt interface of the 2 nm thick $HfO_2$/InP and the drastic increase in film thickness after PDA indicate that interfacial reactions are not limited to the interfacial region. Therefore, a large amount of oxidation states of In and P in the 11 nm thick $HfO_2$ film indicate that $O_2$ that interdiffused through the $HfO_2$ film reacted with In and P atoms that out-diffused into the $HfO_2$ film. The possible reaction mechanism is shown in Figure 6a. In many previous reports, oxygen vacancies were generated easily in crystallized high-$\kappa$ oxide films by thermal treatment or interfacial strain.[18,19] Using secondary ion mass spectrometry (SIMS) and Rutherford backscattering spectrometry (RBS) measurements, the previous studies showed that oxygen vacancies or grain boundaries in crystallized high-$\kappa$ films make the fast diffusion of oxygen possible. Generally, diffusion in solid-state crystals occurs either because of interstitial or substitutional diffusion mechanisms. In particular, in substitutional diffusion, the diffusant migrates from point vacancy to point vacancy rapidly in the crystal solid state. Moreover, the activation energy for diffusion is reduced by pre-existing vacancies or grain boundaries. Therefore, fast diffusion of oxygen through $HfO_2$ is possible along vacancies during the PDA process, as shown in Figure 6a. Similar to oxygen interdiffusion, out-diffusion of atomic In and P can occur at annealing temperatures higher than the dissociation temperature of InP, ~300 °C. In contrast, in $HfO_2$/InP after PDN, interdiffusion and out-diffusion were suppressed. The most possible cause of suppression is that nitrogen occupying the oxygen vacancy sites in crystalline $HfO_2$ film blocked the interdiffusion sites, as shown in Figure 6b. The chemical-bonding state based on XPS analysis and distribution of nitrogen based on SIMS strongly support the role of incorporated nitrogen in the film. We did not find any evidence of chemical reaction of Hf 4f and N 1s core-level spectra in the XPS data. That is, incorporation of N into $HfO_2$ film was not caused by chemical bonding between N and $HfO_2$. Considering the chemical state of N 1s as determined from XPS data and the depth profile of nitrogen based on SIMS data, we speculate that ionized $NH_x$ bonded to oxygen vacancies in $HfO_2$. The change in oxidation states of $HfO_2$/InP after PDA and PDN indicated that interfacial reactions were significantly suppressed in PDN samples and that reaction features of PDN were different from those of PDA. The interfacial reaction mechanism affects the formation of interfacial oxides (i.e., the $InPO_4$ state was dominant after PDA, whereas the $In(PO_3)_3$ and $In_2O_3$ states were dominant after PDN). Interfacial oxides in $HfO_2$/InP were produced as following two steps[5]

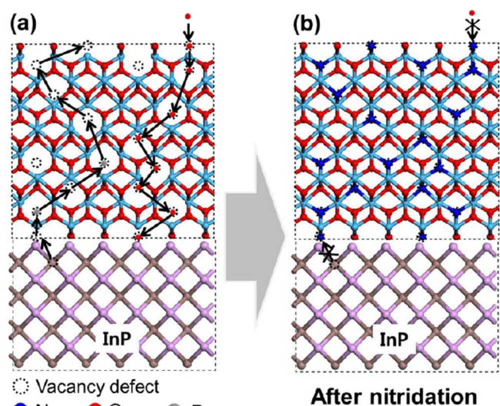


**Figure 6.** Schematic diagrams of interfacial reactions and diffusion models for both (a) as-grown and (b) postnitridation samples.

(i) Formation of $In_2O_3$ and $In(PO_3)_3$: $3InP + 6O_2 \rightarrow In_2O_3 + In(PO_3)_3$ ($\Delta G \sim -753.4$ kcal/mol);

(ii) Formation of $InPO_4$ from $In_2O_3$ and $In(PO_3)_3$: $4In_2O_3 + 8P \rightarrow 5InP + 3InPO_4$ ($\Delta G \sim -158.6$ kcal) and $8In + 4In(PO_3)_3 \rightarrow 3InP + 9InPO_4$ ($\Delta G \sim -198$ kcal).

According to the equilibrium phase diagram of the In−P−O ternary system, four oxidation states, $In_2O_3$ ($\Delta G \sim -198.6$ kcal/mol), $In(PO_3)_3$ ($\Delta G \sim -610$ kcal/mol), $InPO_4$ ($\Delta G \sim -287$ kcal/mol), and $P_2O_5$ ($\Delta G \sim -322.4$ kcal/mol), can be initially formed at room temperature as native oxides of InP. In particular, this report indicated that the conversion of $In_2O_3$ and $In(PO_3)_3$ to $InPO_4$ could occur under sufficient thermal energy according to the above equation. The produced InP immediately dissociated to In and P atoms in step 2, which are also sources for oxidation. In step 2, elemental In or P is needed

for the formation of $InPO_4$. Because nitridation in $HfO_2$ film suppresses the out-diffusion of In and P, $InPO_4$ states are not detected in $HfO_2$/InP after PDN, as compared to $HfO_2$/InP after PDA. In addition, according to the earlier-shown chemical equation, more $In_2O_3$ is consumed than $In(PO_3)_3$ to form the $InPO_4$ sate after PDA, indicating that diffusion of In is harder than that of P because of the larger atomic size of In. In the 2 nm thick $HfO_2$/InP obtained after PDA, massive In-oxide and P-oxide states were measured because of considerable diffusion of In and P through $HfO_2$, as confirmed by TEM. Moreover, in the 2 nm thick $HfO_2$/InP after PDN, $In_2O_3$ states were consumed to form InN by the following chemical equation

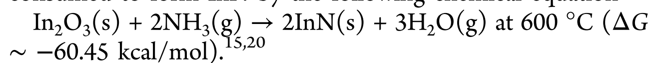

$In_2O_3(s) + 2NH_3(g) \rightarrow 2InN(s) + 3H_2O(g)$ at 600 °C ($\Delta G \sim -60.45$ kcal/mol).[15,20]

Although the peak height of P 2p was significantly smaller, the reaction features of the In 3d spectra are consistent with the results obtained for the P 2p spectra (Supporting Information Figure S3). The decrease in peak height of the generated oxide layer is due to the difference in the surface sensitivity between P 2p and In 3d (i.e., because the surface sensitivity of P 2p is ~10 times lower than that of In 3d based on XPS measurements, interfacial oxide was not detected in the P 2p core-level spectra of 11 nm thick $HfO_2$ film after PDN), as shown in Supporting Information Figure 3c. There is more evidence of the reaction control mechanism in Figure 6. We sought to compare and analyze the 2 nm thick $HfO_2$/InP samples using XPS to clarify the reaction control mechanism, as shown in Supporting Information Figure 4. As mentioned earlier, In and P oxidation states are significantly decreased after PDN at 600 °C as compared to the PDA sample. Similarly, In and P oxidation states are significantly decreased after PDN at 500 °C, as shown in Supporting Information Figure 4. However, in N 1s core-level spectra of the 2 nm thick $HfO_2$/InP, InN bonds were not detected after RTN at 500 °C, whereas the InN peak was clearly visible after RTN at 600 °C. However, $NH_x$ states can still be observed after RTN at 500 °C. The results indicated that the $NH_x$ incorporated into the $HfO_2$ film was the main suppressor of the formation of oxidation states. As a result, we carefully propose that the $NH_x$ incorporated into the $HfO_2$ film was the main suppressor of the formation of oxidation states and acted by effectively blocking In or P out-diffusion.

Energy-band parameters such as band gap ($E_g$), conduction band offset (CBO), and valence band offset (VBO) need to be known to evaluate the band alignment in MOS gate-stack structures. Energy-band alignments can be obtained from the combination of valence band (VB) spectra and reflection electron energy-loss spectroscopy (REELS), as shown in Figure 7. $E_g$ can be defined as the threshold energy of band-to-band excitation, as shown in the REELS spectra in Figure 7a. We evaluated the band gap within ~1.7 nm in the depth direction using an incident electron-beam energy of 1 keV because the mean free path of electrons in $HfO_2$ is ~1.7 nm. The measured optical $E_g$ of $HfO_2$ was 5.8 ± 0.2 eV, which is almost same as the reported value. To measure VBO between $HfO_2$ and InP, VB spectra were obtained for the as-grown 2 nm thick $HfO_2$/InP sample, as shown in Figure 7b. The difference in the valence band maximum (VBM) value between $HfO_2$ and InP resulted in a VBO value of ~2.3 eV. We calculated the effective electron-barrier height, CBO, using the following equation: CBO = $E_g^{\text{oxide}} - E_g^{\text{InP}}$ − VBO. Finally, the energy-band diagram of the as-grown $HfO_2$/InP is shown in Figure 7d. There was a decrease in VBO after PDN of 2 nm thick $HfO_2$/InP. The smaller VBO after nitridation is due to the electronic structure

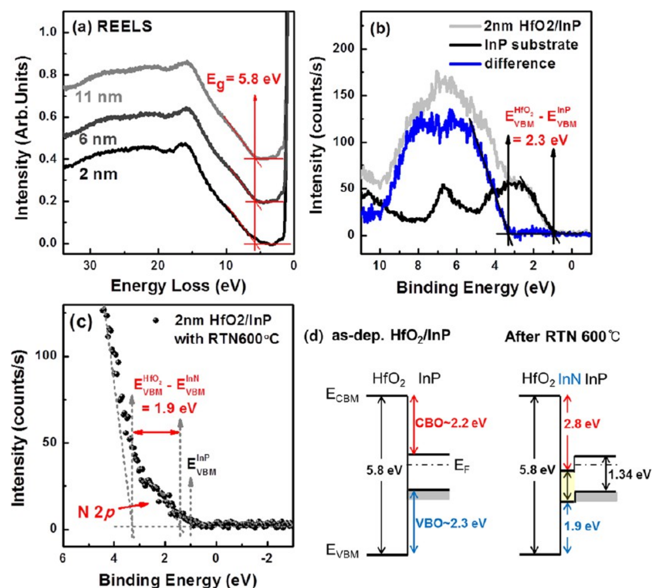


**Figure 7.** (a) REELS spectra for energy band gaps of the 2, 6, and 11 nm $HfO_2$ films. (b) Valence band spectra of both as-grown 2 nm $HfO_2$/InP and (c) 2 nm $HfO_2$/InP after rapid thermal nitridation. (d) Schematic band diagrams of $HfO_2$/InP before and after nitridation.

of interfacial InN, as indicated by the red arrow in Figure 7c. The energy-band diagram of $HfO_2$/InP after PDN is displayed in Figure 7d. In the $HfO_2$/InP system, nitridation (i) decreased the effective hole-barrier height to ~0.4 eV and (ii) increased the effective electron-barrier height to ~0.6 eV.

Figure 8a shows the leakage-current characteristics for substrate electron injection (positive voltage) and gate electron injection (negative voltage) in the 11 nm thick $HfO_2$/InP before and after postannealing. $I-V$ features are sensitive indicators of the characteristics of films and interfaces, such as defect states and the barrier height between $HfO_2$ and InP. A low current level on the order of $\sim 10^{-8}$ was maintained up to ~2 V in both the as-grown and PDA samples, whereas this current level was maintained up to ~4 V by nitridation. This phenomenon was caused by an increase in electron-barrier height. To determine the barrier height of $HfO_2$/InP, we performed fitting using Fowler−Nordheim (F−N) tunneling characteristics in the high-field region, as shown in Figure 8b. F−N tunneling of an electron or hole can be expressed using $J/E^2 = A\exp(-B/E)$. Tunneling characteristics were investigated using a plot of $\ln(J/E^2)$ vs $1/E$, or a so-called a F−N plot, where $J$ is the current density in A cm$^{-2}$, $E$ is the electric field in V cm$^{-2}$, and pre-exponent $A$ and the slope $B$ are given by $A = (e^3 m)/(16\pi^2\hbar m_{ox}\varphi_0)$ and $B = {}^4/_3((2m_{ox})^{1/2})/(e\hbar)\varphi_0^{3/2}$ (V cm$^{-2}$), where $e$ is the electronic charge, $m$ is the free electron mass, $m_{ox}$ is the electron or hole mass in the oxide, $2\pi\hbar$ is Planck's constant, and $\varphi_0$ is the effective barrier height. The barrier height of as-grown and PDA samples was ~2.2 and 2.1 eV, respectively, with an effective mass of 0.3 $m_0$ (data for the PDA sample are not shown in this article). The effective barrier height of ~2.2 eV for the as-grown sample is consistent with the CBO value shown in the previous band diagram in Figure 7d. Two different CBO values of 2.8 (orange line) and 2.5 eV (pink line) were obtained for $HfO_2$/InP after PDN, indicating that a new defect state located at ~0.4 eV below the CBM of $HfO_2$ was generated in the nitrided $HfO_2$ film in the high-field region over 5.4 V. The leakage-current level of the PDN sample was higher than that of the as-grown sample in the negative

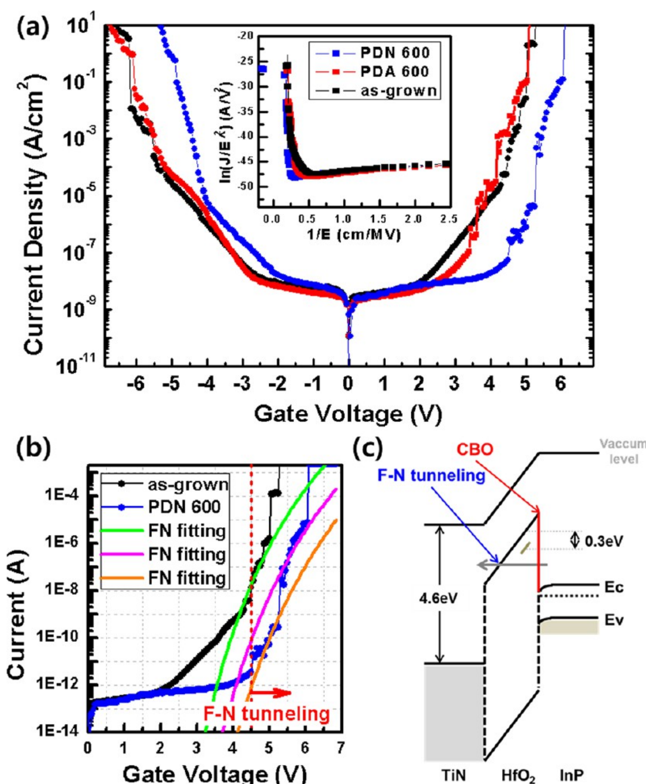


**Figure 8.** (a) Leakage-current−voltage characteristics for the 11 nm $HfO_2$ film on InP with a TiN top electrode. The inset shows F−N plots obtained from $I-V$ measurements. (b) $I-V$ simulation of 11 nm $HfO_2$/InP in the F−N tunneling region to evaluate the barrier height between the $HfO_2$ film and InP semiconductor. (c) Schematic band diagram of the MOS structure.

voltage sweep. This indicates that the effective barrier height for holes was decreased by nitridation; this was also supported by the decreasing VBO shown in the band diagram in Figure 7d.

Frequency-dependent $C-V$ curves as a function of ac frequency were evaluated in the 11 nm thick $HfO_2$/InP before and after thermal annealing to investigate the net charge density of oxide traps near the interface, which are referred to as border traps (Figure 9a−d). Border-trap density was calculated from the capacitance difference during forward and reverse $C-V$ sweeps at 100 kHz as $[C_{rf} = |C_r - C_f|]$, where $C_r$ and $C_f$ are the capacitance density during the reverse and forward sweep, respectively. In the $HfO_2$/InP system, multiple oxidation states such as $In_2O_3$, $In(PO_3)_3$, and $InPO_4$ can be considered to be trap sources. Although oxidation states caused by interfacial reactions increased greatly after PDA, the border-trap density in as-grown $HfO_2$/InP did not change after PDA. These results indicate that multiple oxidation states are not the main source for border traps. However, the border-trap density decreased substantially after nitridation. Therefore, we conclude that the most possible source for the border trap is oxygen vacancy in the $HfO_2$ film and that nitridation is very effective at lowering the border-trap density. The equivalent oxide thickness (EOT) of the as-grown $HfO_2$ film was calculated using as-grown $HfO_2$ samples of various thicknesses, as shown in Figure 9e. On the basis of the linear fit line at 100 kHz ac frequency, we obtained a dielectric constant of ∼14 for the as-grown $HfO_2$. In addition, an equivalent oxide thickness (EOT) of ∼1.6 nm was obtained for the 6 nm thick $HfO_2$/InP film. Accumulation capacitance increased in $HfO_2$/InP after PDA as compared with the as-grown sample. This result indicated that the $HfO_2$ film after PDA had a higher permittivity than the as-grown sample because of enhancement of long-range ordering of $t$-$HfO_2$, as shown in the XRD data. However, because the crystal structure of $t$-$HfO_2$ transformed to the mixture structure of $m$-$HfO_2$ and

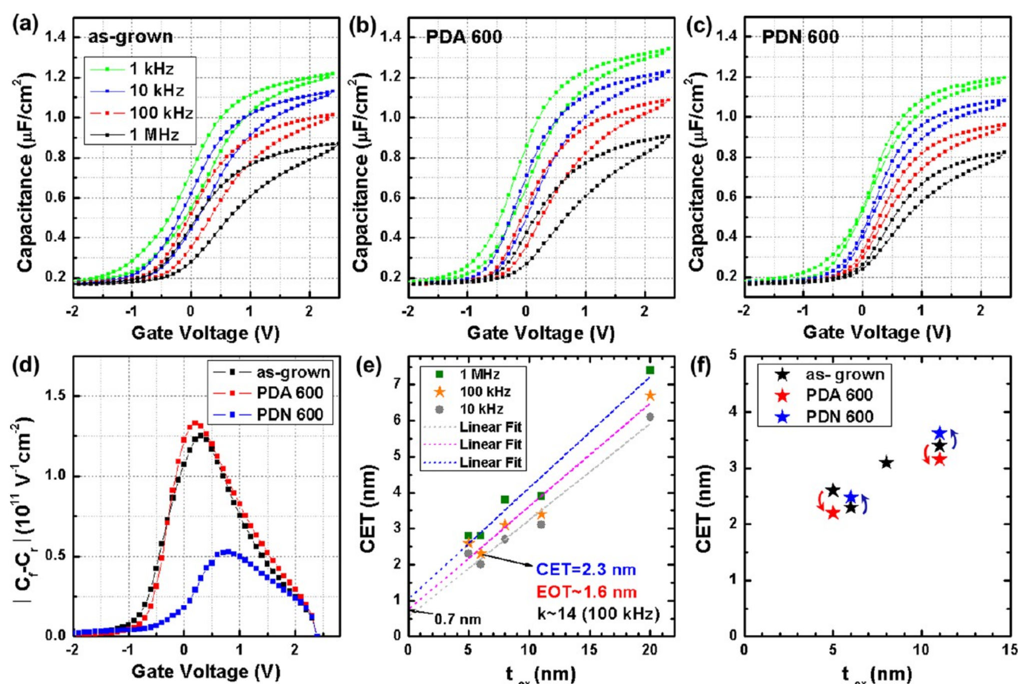


**Figure 9.** (a−c) $C-V$ curves of the MOS structure with a TiN top electrode at several frequencies before and after thermal nitridaion. (d) Effective border-trap density of 11 nm $HfO_2$ before and after thermal nitridation as a function of gate voltage. CET values for (e) as-grown $HfO_2$/InP and (f) annealed $HfO_2$/InP as a function of dielectric thickness.


dx.doi.org/10.1021/am4049496 | ACS Appl. Mater. Interfaces 2014, 6, 3896−3906

$t$-$HfO_2$ after nitridation, the permittivity of the film with a mixture structure did not increase, as shown in Figure 9f.

The interface trap density ($D_{it}$) of $HfO_2$/InP before and after thermal annealing as well as capacitance ($C_m$) and conductance ($G_m$) were determined, as shown in Supporting Information Figure 5. Figure 10a shows the trap energy level given by Shockley−Read−Hall statistics for the capture and emission rates. To measure the energy level of the defect states from 0.25 to 1.13 eV from the valence band edge of InP, $C_m$ and $G_m$ were obtained using S-doped n-type and Zn-doped p-type substrate under the following measurement conditions: frequency between 1 and 1000 kHz and a temperature of 25 or 200 °C. In $HfO_2$/InP after PDA, the $D_{it}$ at ∼0.7 eV from the valence band edge increased significantly from $1.0 \times 10^{13}$ to $1.1 \times 10^{14}$ $eV^{-1}$ $cm^{-2}$ because of out-diffusion of In and P, as reported in a previous study.[21] However, $D_{it}$ increased slightly from $1.0 \times 10^{13}$ to $3.5 \times 10^{13}$ after thermal nitridation using $NH_3$, which supports our finding that nitridation controls the out-diffusion of In and P. However, after nitridation, the generation of a new defect state at ∼0.5 eV within the InP band gap was observed, as indicated by the black arrow in Figure 10b. This was likely caused by In−N bonding at the $HfO_2$/InP interface. More detailed theoretical and experimental analyses are required to determine the origin of this ∼0.5 eV defect state.

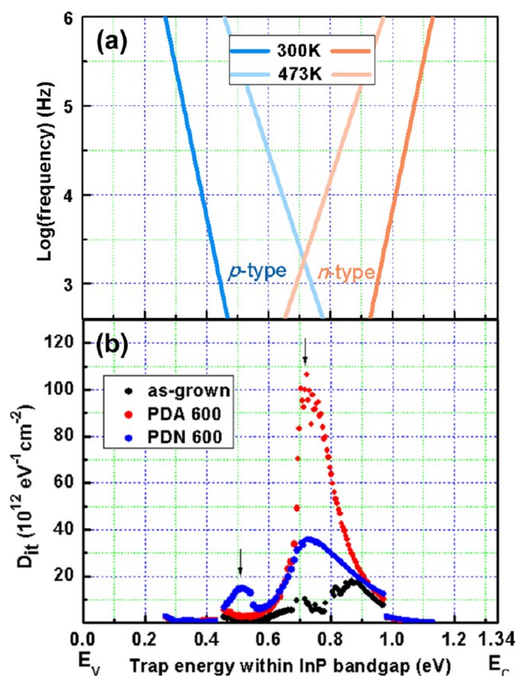


**Figure 10.** (a) Relationship between electron-trap energy levels and working frequency based on $C$−$V$ measurements. (b) Conductance results for $HfO_2$/InP before and after thermal nitridation. For wide-range measurements, both n-type and p-type InP substrates were used. and samples were measured at temperatures of 25 and 200 °C.

We performed DFT calculations to confirm the defect states of In and P impurities in $HfO_2$. Figure 11a shows the atomic structure of $t$-$HfO_2$ containing interstitial In ($In_i$) or P ($P_i$) in $HfO_2$ after geometrical optimization (first, pure $t$-$HfO_2$, second, $In_i$ in $HfO_2$, and third, $P_i$ in $HfO_2$). In the case of both $In_i$ and $P_i$, structural deformation was observed around the interstitial atoms. We calculated the total density of states (TDOS) for $In_i$ and $P_i$ inside $t$-$HfO_2$ films by considering the various charged states shown in Figure 11b,c. We observed energy states generated between the valence band and the Fermi energy level, as indicated by arrows. According to the TDOS for perfect $t$-$HfO_2$, occupied states below the Fermi level were composed of bands of O 2p states and Hf 5d states created as a result of covalent bonding between Hf and O atoms. Unoccupied states were induced from spin−orbit coupling between the O 2p orbitals and electrons of Hf 5d and 6s. There were no gap states in pure $t$-$HfO_2$ film, whereas many gap states

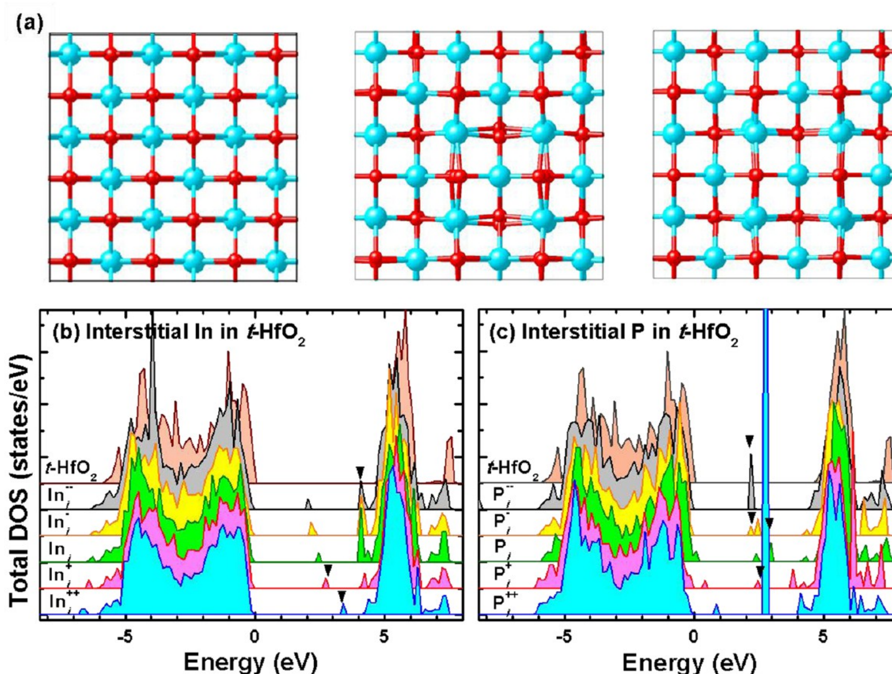


**Figure 11.** (a) Atomic structures of $t$-$HfO_2$ (002) for defect-free $HfO_2$, interstitial In in $HfO_2$, and interstitial P in $HfO_2$ (red, =oxygen; blue, hafnium). Total density of states for (b) In interstitial- and (c) P interstitial-related defect states in $t$-$HfO_2$.

were produced in $t$-$HfO_2$ films containing In or P impurities. In particular, $P_i$ in $HfO_2$ had a more intense midgap state than $In_i$ in $HfO_2$. These changes could be induced by local symmetry distortions or changes in the local coordination of $In_i$ or $P_i$. Energy-band diagrams after scissoring correction of defect states related to $In_i$ or $P_i$ in $t$-$HfO_2$ are displayed in Figure 12.

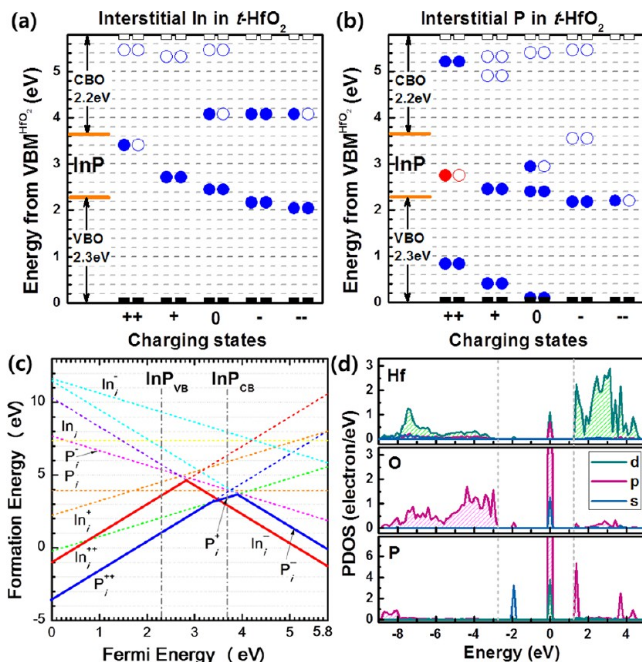


Figure 12. (a, b) Energy-band diagram of interfacial defect states for $t$-$HfO_2$/InP. The filled circles and open circles correspond to occupied states and unoccupied states, respectively. (c) Formation energies versus Fermi energy for In or P impurities in $t$-$HfO_2$. (d) Partial density of states in the case of the interstitial $P^{2+}$ charged state in $t$-$HfO_2$.

Band alignments for $t$-$HfO_2$ film/InP were assumed from the previous band diagram shown in Figure 7d. To find states with the lowest formation energy, formation energies for various charged states of $In_i$ or $P_i$ inside the $t$-$HfO_2$ film were calculated as shown in Figure 12c. Formation energies for both $In_i$ and $P_i$ in $t$-$HfO_2$ were high (positive values) (i.e., out-diffusion of In or P into $t$-$HfO_2$ film was not easy). Therefore, there is another reason for the out-diffusion of In or P into $t$-$HfO_2$ film during annealing. That is, the presence of defects such as oxygen vacancies and grain boundaries critically enhance out-diffusion in a real system, as mentioned in Figure 6. Considering the lowest formation energy in the band gap of InP, $P_i^{+2}$, $P_i^{+}$, $In_i^{+}$, and $In_i^{-2}$ charged states are possible in the $t$-$HfO_2$ film because of the energetically stable gap state of InP. Interfacial defect states located at ~0.7 eV from the VBM of InP measured by the conductance method are consistent with defects caused by $P_i^{+2}$ or $In_i^{+}$ in $t$-$HfO_2$. The partial density of states (PDOS) was calculated for the most possible case, $P_i^{+2}$ in $t$-$HfO_2$, as shown in Figure 12d. These results indicate that $P_i^{+2}$ in $t$-$HfO_2$ produced defect states in the band gap of $HfO_2$, which originated mainly from the s-orbital of P for lower-energy states and the p-orbitals of P for higher-energy states. From DFT and experimental results, we expected that portions of the out-diffused InP substrate elements would react with oxygen, resulting in In−P−O formation. Some of the out-diffused In and P remained as interstitial In ($In_i$) or interstitial P ($P_i$) in $HfO_2$ dielectric or near the InP substrate during thermal annealing at 600 °C, however. $In_i$ and the $P_i$ near the InP substrate resulted in degradation of carrier mobility because of an increase in Coulomb scattering. Because the out-diffusing of In or P was suppressed by thermal nitridation, we conclude that device thermal stability can be improved by using $NH_3$ ambient gas during the postannealing process.

## IV. CONCLUSIONS

We investigated the effects of postnitridation annealing using $NH_3$ vapor on the structural and electrical properties of $HfO_2$ thin films deposited on InP by ALD and compared the structural and electrical properties of these films to those of $HfO_2$/InP films synthesized with PDA using $N_2$ vapor. After the nitridation process, an InN layer was produced at the $HfO_2$/InP interface, and ionized $NH_x$ bonded to defect states in $HfO_2$. As a result, interfacial reactions were effectively suppressed in nitrided $HfO_2$/InP by controlling out-diffusion of In or P atoms from the substrate. Nitridation of $HfO_2$/InP modulated energy-band parameters at the $HfO_2$/InP interface, thereby decreasing leakage current. Moreover, the nitridation process significantly suppressed the generation of $D_{it}$ because of the controlled diffusion of In and P. DFT calculations showed that $In_i$ and $P_i$ in $HfO_2$ are closely related, with defect states within the band gap of InP.

## ASSOCIATED CONTENT

### Supporting Information

TOF-SIMS depth profiles of Hf, O, In, P, and N; cross-sectional HR-TEM images of a $HfO_2$ film on InP after rapid thermal annealing in a $N_2$ ambient as a function of film thickness; XPS core-level spectra as a function of film thickness and annealing treatment; and multifrequency $C-V$ characteristics and normalized parallel conductance in MOS capacitors of 11 nm $HfO_2$ film on InP before and after rapid thermal annealing. This material is available free of charge via the Internet at http://pubs.acs.org.

## AUTHOR INFORMATION

### Corresponding Author

*E-mail: mh.cho@yonsei.ac.kr.

### Notes

The authors declare no competing financial interest.

## ACKNOWLEDGMENTS

This work was partially supported by an Industry−Academy joint research program between Samsung Electronics−Yonsei University and by a grant, Next-Generation Substrate Technology for High Performance Semiconductor Devices (no. KI002083), from the Ministry of Knowledge Economy of Korea.

## REFERENCES

(1) Robertson, J.; Falabretti, B. *Mater. Sci. Eng., B* **2006**, *135*, 267.
(2) Kang, Y.-S.; Kim, D.-K.; Cho, M.-H.; Seo, J.-H.; Shon, H. K.; Lee, T. G.; Cho, Y. D.; Kim, S.-W.; Ko, D.-H.; Kim, H. *Phys. Status Solidi A* **2013**, *6*, 211.
(3) Ok, I. J.; Kim, H.; Zhang, M.; Zhu, F.; Park, S.; Yum, J.; Zhao, H.; Garcia, D.; Majhi, P.; Goel, N.; Tsai, W.; Gaspe, C. K.; Santos, M. B.; Lee, J. C. *Appl. Phys. Lett.* **2008**, *92*, 202903.
(4) Dong, H.; Brennan, B.; Zhernokletov, D.; Kim, J.; Hinkle, C. L.; Wallace, R. M. *Appl. Phys. Lett.* **2013**, *102*, 171602.

(5) Kang, Y. S.; Kim, C. Y.; Cho, M.-H.; Chung, K. B.; An, C.-H.; Kim, H.; Lee, H. J.; Kim, C. S.; Lee, T. G. *Appl. Phys. Lett.* **2010**, *97*, 172108.
(6) Dong, H.; Cabrera, W.; Galatage, R. V.; Santosh, K. C.; Brennan, B.; Qin, X.; McDonnell, S.; Zhernokletov, D.; Hinkle, C. L.; Cho, K.; Chabal, Y. J.; Wallace, R. M. *Appl. Phys. Lett.* **2013**, *103*, 061601.
(7) An, C.-H.; Byun, Y.-C.; Cho, M.-H.; Kim, H. *Phys. Status Solidi RRL* **2012**, *6*, 247.
(8) Wang, Y.; Chen, Y.-T.; Xue, F.; Zhou, F.; Lee, J. C. *Appl. Phys. Lett.* **2012**, *101*, 063505.
(9) An, C.-H.; Mahata, C.; Byun, Y.-C.; Kim, H. *J. Phys. D: Appl. Phys.* **2013**, *46*, 275301.
(10) Guo, Y.; Lin, L.; Robertson, J. *Appl. Phys. Lett.* **2013**, *102*, 091606.
(11) Zhang, S. B.; Northrup, J. E. *Phys. Rev. Lett.* **1991**, *67*, 2339.
(12) Chang, C.-H.; Chiou, Y.-K.; Chang, Y.-C.; Lee, K.-Y.; Lin, T.-D.; Wu, T.-B.; Hong, M.; Kwo, J. *Appl. Phys. Lett.* **2006**, *89*, 242911.
(13) Hinkle, C. L.; Sonnet, A. M.; Vogel, E. M.; McDonnell, S.; Hughes, G. J.; Milojevic, M.; Lee, B.; Aguirre-Tostade, F. S.; Choi, K. J.; Kim, H. C.; Kim, J.; Wallace, R. M. *Appl. Phys. Lett.* **2008**, *92*, 071901.
(14) McDonnell, S.; Dong, H.; Hawkins, J. M.; Brennan, B.; Milojevic, M.; Aguirre-Tostado, F. S.; Zhernokletov, D. M.; Hinkle, C. L.; Kim, J.; Wallace, R. M *Appl. Phys. Lett.* **2012**, *100*, 141606.
(15) Kang, Y. S.; Kim, C. Y.; Cho, M.-H.; An, C.-H.; Kim, H.; Seo, J. H.; Kim, C. S.; Lee, T. G.; Ko, D.-H. *Electrochem. Solid State Lett.* **2012**, *15*, G9.
(16) Kumar, S.; Mo, L.; Motlan; Tansley, T. L. *Jpn. J. Appl. Phys.* **1996**, *35*, 2261.
(17) Saitoh, M.; Mizoguchi, T.; Tohei, T.; Ikuhara, Y. *J. Appl. Phys.* **2012**, *112*, 084514.
(18) Brossmann, U.; Wurschum, R.; Sodervall, U.; Schaefer, H.-E. *J. Appl. Phys.* **1999**, *85*, 7646.
(19) Fisher, C. A. J.; Matsubara, H. *Solid State Ionics* **1998**, *113–115*, 311.
(20) Ranade, M. R.; Tessier, F.; Navrotsky, A.; Marchand, R. *J. Mater. Res.* **2001**, *16*, 2824.
(21) Galatage, R. V.; Dong, H.; Zhernokletov, D. M.; Brennan, B.; Hinkle, C. L.; Wallace, R. M.; Vogel, E. M. *Appl. Phys. Lett.* **2011**, *99*, 172901.